

## Research on bearing characteristics of socket-spigot template supporting system

Yan Guo, Chang-Ming Hu\* and Ming Lian

*College of Civil Engineering, Xi'an University of Architecture and Technology, Xi'an 710055, P.R. China*

*(Received April 09, 2015, Revised September 04, 2015, Accepted December 20, 2015)*

**Abstract.** The socket-spigot template supporting system is widely used in engineering applications in China. As a newer type of support structure, there has been growing research interest in its bearing capacity. In this paper, four vertical bearing capacity tests were carried out on the basic mechanical unit frame of a socket-spigot template supporting system. The first goal was to explore the influence of the node semi-rigid degree and the longitudinal spacing of the upright tube on the vertical bearing capacity. The second objective was to analyze the displacement trend and the failure mode during the loading process. This paper presents numerical analysis of the vertical bearing capacity of the unit frames using the finite element software ANSYS. It revealed the relationship between the node semi-rigid degree and the vertical bearing capacity, that the two-linear reinforcement model of elastic-plastic material can be used to analyze the socket-spigot template supporting system, and, through node entity model analysis, that the load transfer direction greatly influences the node bearing area. Finally, this paper indicates the results of on-site application performance experiments, shows that the supporting system has adequate bearing capacity and stability, and comments on the common work performance of a socket and fastener scaffold.

**Keywords:** socket-spigot template supporting system; basic mechanical unit frame; semi-rigid degree; application performance; numerical analysis

---

### 1. Introduction

Recently, reinforced concrete structures have become widely used throughout the construction industry in China. As a temporary support structure, the template supporting system has attracted more attention than ever before. The disadvantages of traditional tube-fastener scaffolds have been gradually revealed, and accident rates are still rising. Outstanding among the disadvantages is the instability of the formwork support system. In order to improve production efficiency and reduce accidents during construction, various types of new formwork support systems, such as cuplock steel tubular scaffold, disk lock steel tubular scaffold, and socket-spigot steel scaffold, have appeared in construction applications during recent years.

Scholars have analyzed the template supporting system extensively over this period. Yu conducted experiments on coupler steel tubular scaffold, cuplock steel tubular scaffold, and gantry scaffold, to determine calculation principles and a safety application mechanism for these scaffold systems, (Yu 2001). Experimental and numerical analysis of four different gantry scaffolds was

---

\*Corresponding author, Ph.D., E-mail: [hu.tm@163.com](mailto:hu.tm@163.com)

conducted, which gave the loading device and loading process, obtained the buckling mode and bearing capacity, predicted the behavior of the tested frames, compared their linear and nonlinear buckling bearing capacities, and pointed out that more study on the safety rate in such applications is required (Weesner and Jones 2001). The influences of geometry-dependent loads and time-dependent incremental loads on various configurations of supporting systems were studied, experimental results were analyzed, and important parameters such as joint stiffness were identified in nonlinear analysis of scaffolds to obtain the response of on-site scaffolds (Peng *et al.* 2007). Load capacities and failure modes of scaffold structures in various construction applications were also researched. The pertinent parameters, including number of stories, ground height, boundary conditions, presence of diagonal bracing, and joint positions were considered in the study, test results and numerical results were discussed, and the importance of joint stiffness on bearing capacities was confirmed (Peng *et al.* 2013). A new safety system to eliminate the risk of workers falling from different heights has been proposed. It is attached to concrete columns, so that the system can be operated in safety, both for the workers and for the integrity of the column itself, (Adam *et al.* 2007). Various site measurements of geometric imperfections in support scaffold systems have been described. These measurements relate to the out-of-straightness of standards, out-of-plumb of the frame, and loading eccentricity between the timber bearer and the U-head screw jack. They represent actual initial geometric imperfections and loading eccentricities encountered in practice (Chandrangsu and Rasmussen 2011a), as well as proposed methods for modeling spigot joints (Chandrangsu and Rasmussen 2011b). A reliability analysis has been presented for typical steel scaffold shoring structures based on the geometric and mechanical properties of steel scaffold members, along with an investigation of the mode of failure, the effects of different random variables on the variability of structural strength, and the reliability of the analyzed scaffold structures (Zhang *et al.* 2012). The provisions for design were examined by advanced analysis, the design of a typical semi-rigid steel scaffold structure was studied using different design-by-advanced analysis methods, and the challenges and need for developing a system-based design methodology using advanced analysis was discussed (Zhang and Rasmussen 2013). Research into scaffold and falsework structures conducted throughout the last forty years was reviewed. Recommendations were made that looseness be considered when new codes are designed, that factors of safety for vertical loads be increased to 2.0, in light of reliability research, and that seismic analysis of template structures be required (Beale 2014).

As seen from this review of the literature, research on steel scaffolding has been extensive, and useful outcomes have been produced, but research on scaffold systems set up as temporary support structures is relatively rare. The few published works that exist provide useful information concerning the ultimate capacity of scaffolding systems, but lack the details required to allow for independent modeling of the tested frameworks.

This paper focuses on the vertical bearing capacity of the unit frame in a socket-spigot template supporting system. The difference between socket-spigot pole connections and tubular pole connections are shown in Fig. 1, it showed the node details of the tested system and steel tubular scaffold with couplers. Experiments combined with numerical analysis are conducted to verify the proposed work. Initially, a bearing capacity experiment is conducted on four unit frames of a socket-spigot template supporting system. From this, the ultimate bearing capacity (in this paper, it means the total load on the frame) and the failure modes are obtained. Next, models of the unit frame and the node are established, and numerical analysis is conducted using the finite element software ANSYS. Finally, conducted experiment on site, discussed the application performance of socket-spigot and fastener systems.



(a) Connection of socket-spigot pole



(b) Connection of tubular pole

Fig. 1 Different connections of socket-spigot and tubular pole

## 2. Experimental analysis

### 2.1 Experimental specification and loading pattern

An experiment was conducted on four unit frames of a socket-spigot template supporting system to determine their ultimate vertical bearing capacity. Specifications for each specimen are shown in Table 1. The longitudinal spacing of the upright tubes and the node connection degree were considered as factors that affect the bearing capacity. Their influence on vertical bearing capacity, deformation, and failure mode was analyzed.

The experiment's loading schematic is shown in Fig. 2. The positions of the strain measuring points are shown in Fig. 3, each measuring point had four strain gauges. During the test, the jack,

Table 1 Specification of the unit frames

No.	Lift height/mm	Transverse spacing of upright tube/mm	Longitudinal spacing of upright tube/mm	The node connection degree
1	1200	600	600	Normal wedge tightness
2			600	Minimum wedge tightness
3			1200	Normal wedge tightness
4			1200	Minimum wedge tightness
Height of bottom reinforcing tube/mm				360
Length of stud out/mm				200

The section size of the steel pipe is  $\Phi 48 \text{ mm} \times 2.75 \text{ mm}$ .

The node connection degree is relative to knocking frequency and strength. In testing, knocking 1-3 times with a hammer free falling from a height of 30 cm is considered to be the minimum wedge tightness, knocking 7-10 times with a hammer free falling from 30 cm is considered the normal wedge tightness. There categories generally equate to field procedures where a worker knocking 2 times on the wedge head is considered as minimum tightness, and 8 times is normal tightness.

In the following text, we refer to  $h$  as lift height; refer  $h_1$  as longitudinal spacing of upright tube; refer  $h_2$  as transverse spacing of upright tube, and  $K$  as the node connection degree.

counter-force frame, and loaded beam were used to load the unit frames. The load transfer proceeded from the jack to the second loaded beam, the second loaded beam distributed the load to the primary loaded beams uniformly, which finally passed the load directly to poles in the unit frames. As the load continued to increase, the unit frame eventually deformed, which led to poles separating from the primary loaded beam. To solve this problem, pins attached to the bottom of the primary loaded beam (Fig. 2(b)) were inserted into the poles. As the load grew, the four poles in each unit frame deformed differently, so the loading configuration deviated. At this point, the pins on the primary loaded beam that connected the loading device with the poles to prevent the instability caused by small deformation, caused the unit frame to continue bearing load until it failed by ultimate load or large deformation.

Loading proceeded in 20 kN increments, with pauses to observe and read the displacement transducers. After the readings stabilized, loading increased. This cycle continued until failure,

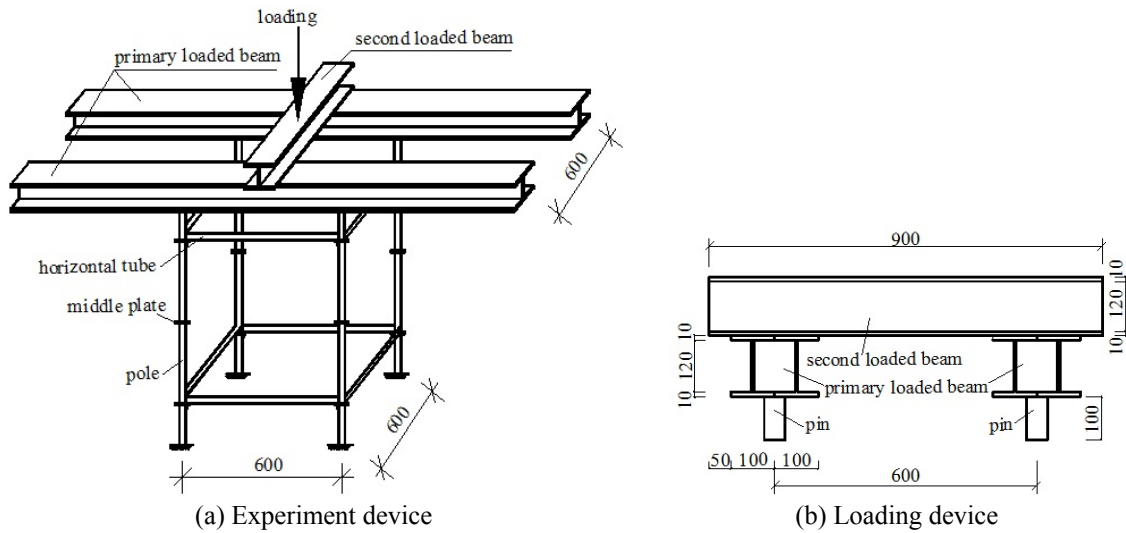


Fig. 2 The loading schematic diagram

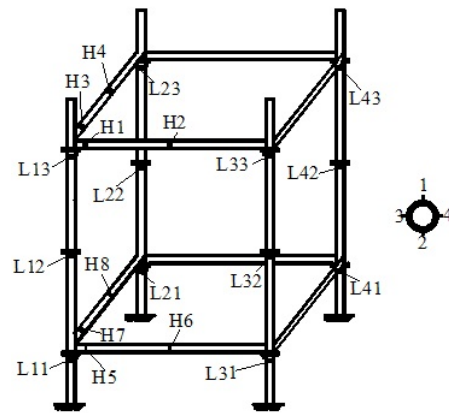


Fig. 3 Positions of strain measuring points

when displacements changed rapidly. Components are in contact with each other in a template supporting system. To improve the unloaded unit frame’s stability, it was fixed to a ground beam during the experiment.

**2.2 Experimental results and analysis**

**2.2.1 Ultimate vertical bearing capacity**

Experimental observations were used to obtain the ultimate vertical bearing capacity for each of the four unit frames. All of the collected data is listed in Table 2.

As shown in that table, different combinations of  $h_1$  and  $K$  suggest the following relationships: the ultimate vertical bearing capacity of specimen 1, with a small  $h_1$  and a large  $K$ , is the largest, while the ultimate vertical bearing capacity of specimen 4, with a large  $h_1$  and a small  $K$ , is the least. In contrast, the vertical bearing capacity is reduced 24% when  $K$  is reduced for a specimen with a small  $h_1$ , whereas it is reduced 53% when  $K$  is reduced for a specimen with a larger  $h_1$ . When  $h_1$  is increased, the ultimate vertical bearing capacity is reduced 50% for a specimen with a large  $K$ , and 85% with a small  $K$ . This points out that the larger  $h_1$  is, the smaller the vertical bearing capacity is, and that the larger  $K$  is, the larger the vertical bearing capacity is.

The above analysis shows that  $h_1$  is the major factor that affects the vertical bearing capacity, rather than  $K$ , while the influence of  $K$  on the vertical bearing capacity is dependent on  $h_1$ , and the impact of it is more obvious with a larger  $h_1$ .

**2.2.2 Displacement and buckling mode of the unit frames**

The displacement of the middle plate (as shown in Fig. 2) was recorded during the experiment; the displacement transducers are shown in Fig. 4. In this figure, the east-west direction is considered to be the X axis and the south-north direction to be the Y axis.

Table 2 Experimental results of the ultimate vertical bearing capacity

Item	①	②	③	④
No.	1	2	3	4
Bearing capacity/kN	351	283	234	153
Compare item	(①-②)/②	(③-④)/④	(①-③)/③	(②-④)/④
Compare value	24%	53%	50%	85%



Fig. 4 Arrangement of displacement transducers

The displacement transducers slide out when the unit frame is damaged. They cannot record the displacement during the unloading process. Therefore, we drew the displacement curve of each pole during the loading process in Fig. 5.

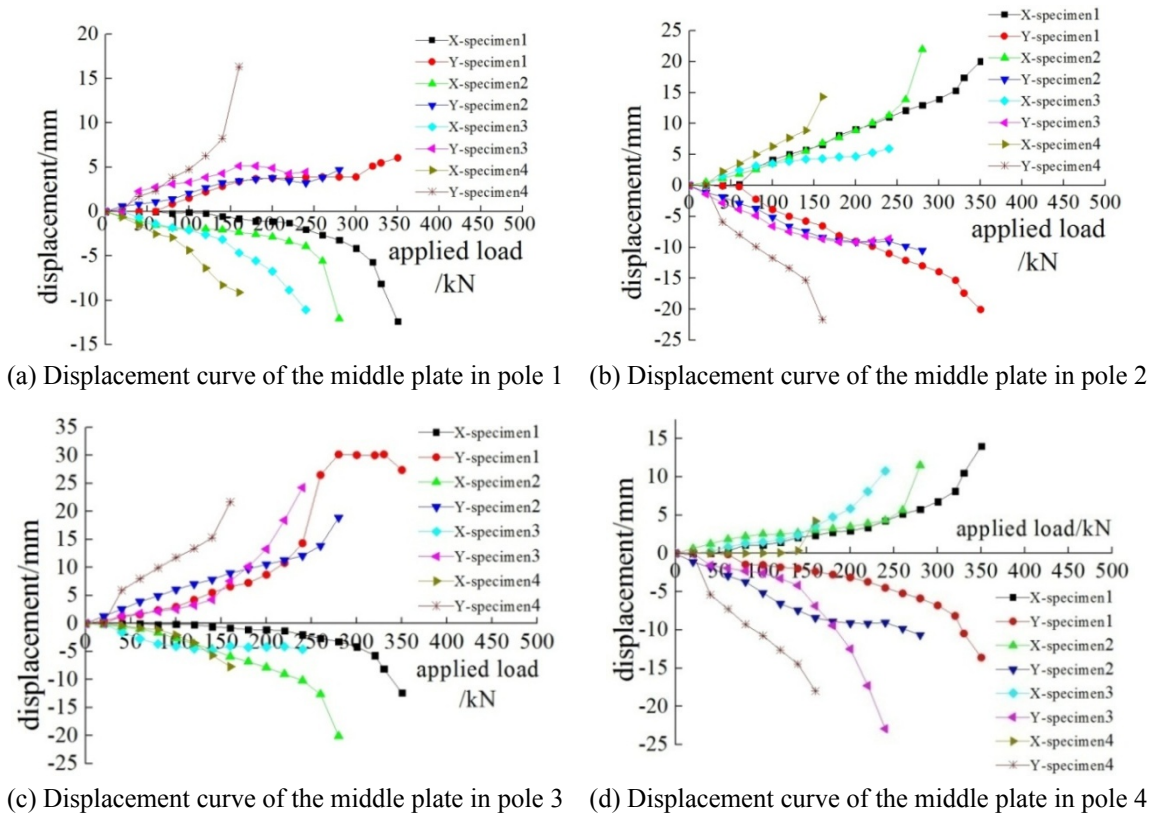


Fig. 5 Displacement curve of the middle plate during loading process



(a) Buckling mode of specimen 1



(b) Buckling mode of specimen 2

Fig. 6 Buckling mode of the unit frame



(c) Buckling mode of specimen 3



(d) Buckling mode of specimen 4

Fig. 6 Continued

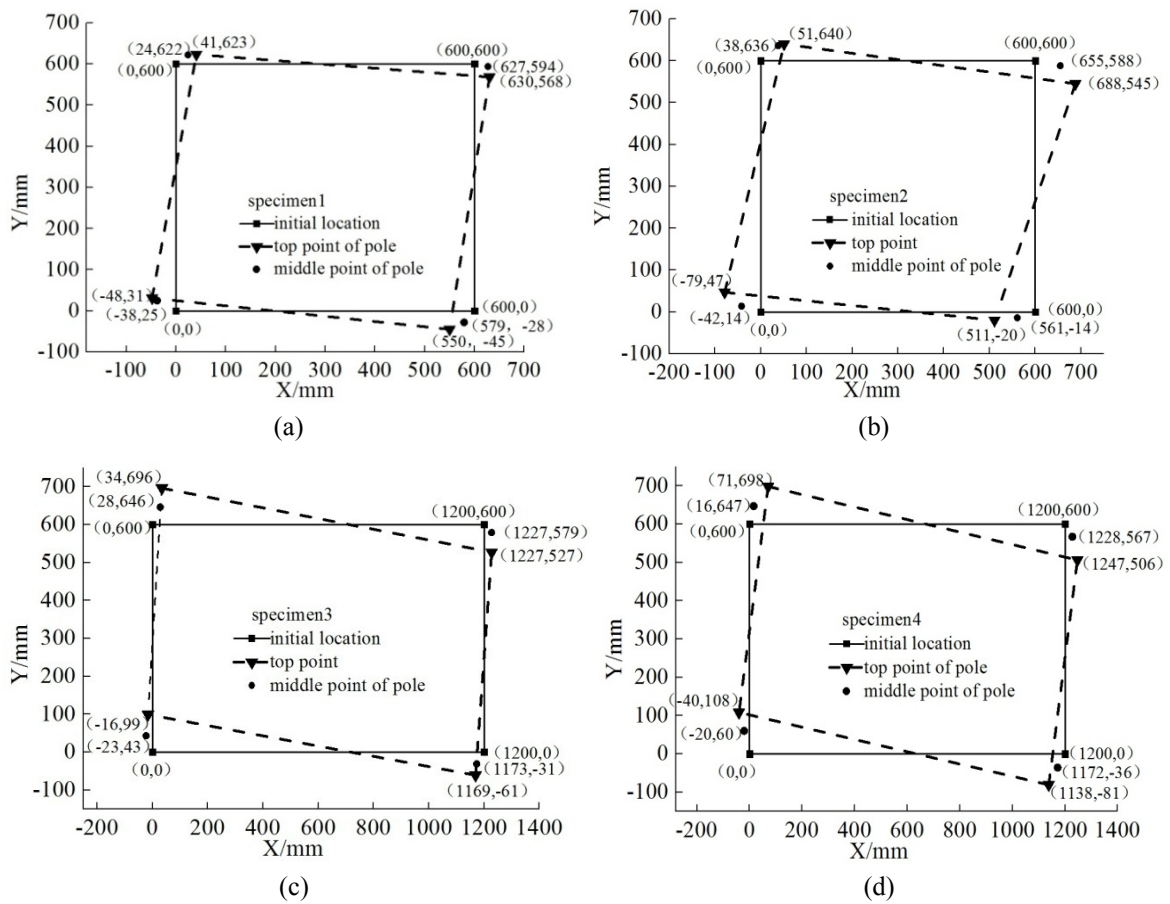


Fig. 7 The pole displacement in unit frame after completely unloaded

The displacement curves show that the displacement trend remains roughly the same at the corresponding positions, although the specimens are different. The Y displacement of specimen 4 grew fast during the initial loading process, and the displacement increased significantly when the unit frame was close to being destroyed. Different values of  $h_1$  and  $K$  for the specimens led to different displacement trends during the loading process and the final destroyed displacement. The displacement increased slowly with a small  $h_1$  and large  $K$ , while the displacement increased in a certain degree as  $h_1$  increased and  $K$  decreased.

The buckling mode of each unit frame is shown in Fig. 6. All the specimens were destroyed with clockwise torsion. However, different  $h_1$  and  $K$  values led to different torsional angles.

The displacement of the middle point and top point of each pole is gathered in a plan view, Fig. 7. In it, the poles look like dots, ■ refers to the initial position of the poles, and ▼ and ● refer to the top and middle points of each pole, respectively, after being completely unloaded. The lines between the symbols are horizontal tubes. The coordinate points are relative, but they intuitively show the displacement of each unit frame.

From Fig. 7, all the specimens were destroyed with clockwise torsion, even though their erection was different from each other. The X and Y resistant-lateral stiffness were the same in specimens 1 and 2, which had the same  $h_1$ . Hence, the X and Y displacements are similar for those two specimens, while the Y resistant-lateral stiffness was very different from X in specimens 3 and 4, which had a longitudinal distance twice as long as the horizontal distance. Therefore, the weak side's displacement was larger than the strong side's. Analysis confirms that the clockwise torsion of each specimen was caused by the same external conditions, namely the loading device. The loading step is the same during the tests, and the specimens would have been twisted in the opposite direction if the external conditions had been changed.

The wedge head slid a little bit during the loading process, and led to the pole strain mutation. As the loading process was carried out on the unit frame, the wedge head slid easily with a small node connection stiffness, which caused the frame to twist. Subsequent weight imbalances on the poles led to further sliding of the wedge head. During the loading process, the wedge head slid out of specimen 4 when the other side twisted, hence, it could no longer carry the load and its bearing capacity was the least. In engineering applications, special attention should be paid to node connection stiffness to prevent accidents caused by the wedge head sliding out.

### 2.2.3 Node stiffness of the unit frames

The node stiffness is derived through the unit frame test by measuring the horizontal tube strain (H1, H3, H5, and H7 shown in Fig. 3) at a distance of 50 mm from the primary node, and recording the torsional displacement at each loading level. The derivation is as follows:

$$\text{Strain results: } \varepsilon = \frac{1}{2}(|\varepsilon_1| + |\varepsilon_2|)$$

$$\text{The calculation formula of moment: } \sigma = \frac{M}{W}$$

$$\text{While, } \sigma = E\varepsilon$$

$$\text{So, } M = \frac{1}{2}EW(|\varepsilon_1| + |\varepsilon_2|)$$

In these equations,  $\varepsilon$  is strain,  $\varepsilon_1$  and  $\varepsilon_2$  are the measured strain of 1 and 2 as shown in Fig. 3,  $\sigma$  is stress,  $M$  is moment,  $W$  is section modulus, and  $E$  is elastic modulus.

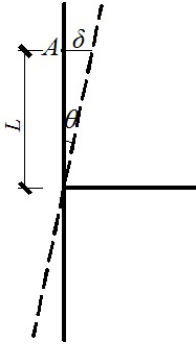
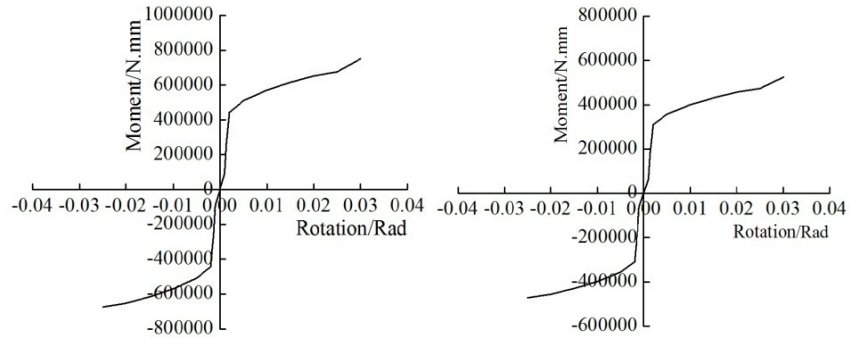


Fig. 8 The relative rotation calculation diagram



(a) The normal wedge tightness (b) The minimum wedge tightness  
Fig. 9  $M-\theta$  curve of the node

The calculation formula of relative rotation:  $\theta = \frac{\delta}{L}$

In this equation,  $\theta$  is rotation,  $\delta$  is torsional displacement,  $L$  is the distance between main node and measuring point, as shown in Fig. 8.

For each test, we recorded the strain of each strain gauge, so we could easily obtain the bending moment of measuring points H1, H3, H5, and H7. We recorded torsional displacement with displacement transducers, so we were able to calculate the node rotation. Then we calculated the node stiffness using the above parameters.

Lastly, we drew the  $M-\theta$  curve of the node in Fig. 9.

### 3. Numerical analysis

#### 3.1 Numerical models of unit frames

Numerical analysis was conducted using the finite element software ANSYS. In the analysis, the BEAM188 and COMBIN39 elements were considered to simulate the tubes and the connections, respectively. The steel material properties in the simulation were obtained by a unilateral tensile test. The test data are shown in Table 3. The stress-strain curves of the three tests are shown in Fig. 10.

We obtained the yield stress  $\sigma_s$ , yield strain  $\varepsilon_s$ , ultimate stress  $\sigma_u$ , and ultimate strain  $\varepsilon_u$ , from the unilateral tensile test, and the tangent modulus  $E_t$  is  $E_t = \frac{\Delta\sigma}{\Delta\varepsilon} = \frac{\sigma_u - \sigma_s}{\varepsilon_u - \varepsilon_s}$ . So calculate  $E_t$  by

the above data and formula. It shows that  $E_t \approx 0.01E$ , where  $E$  is the elastic modulus of the steel.

In the models, the elasticity modulus, tangent modulus, and Poisson's ratio were assumed to be 221 GPa, 2.21 GPa, and 0.3, respectively. The nonlinear material behavior was modeled using the isotropic hardening rule and the von Mises yield criteria, the two-linear reinforcement model was used to define BEAM188, and the  $M-\theta$  curve showed in Fig. 9 was inputted as the properties of COMBIN39 to simulate the connections.

Free meshing was selected, the element size was defined as 5 mm. As the boundedness of force convergence, the nonlinear analysis will never converge under that, so we define force

Table 3 The material properties of steel

No.	Yield stress/MPa	Ultimate stress/MPa	Elasticity modulus/GPa	Tangent modulus/GPa
1	354	429	194	1.11
2	343	420	240	2.99
3	380	446	229	1.28
Average	359	432	221	1.79

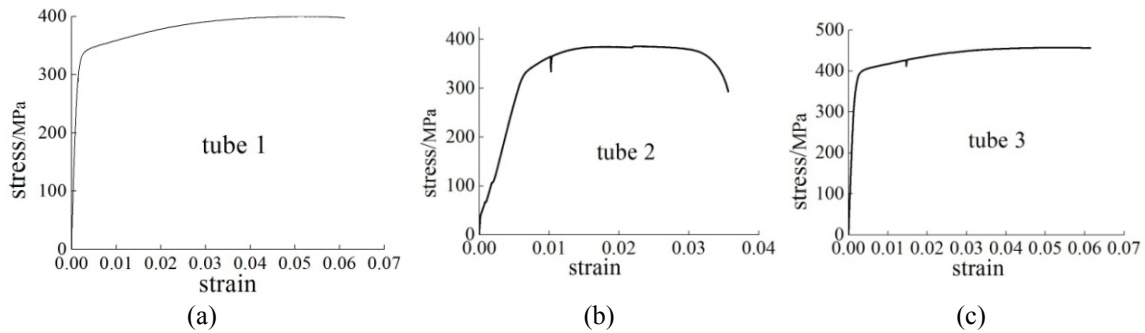


Fig. 10 The stress-strain curves of the tested tubes

convergence and deflection convergence to different elements, the structural elements meshed comply with the force convergence criterion and the node elements meshed comply with displacement convergence criterion. Tolerances were all defined as 0.01 in the nonlinear analysis.

The semi-rigid models are shown in Fig. 11. We counted the pole bottom boundary as a fixed hinge according to the experimental conditions, coupled the translational freedom of the node to consider the actual condition, and coupled the top vertical displacement of all the poles in nonlinear buckling analysis to consider the central loading condition of the experiment.

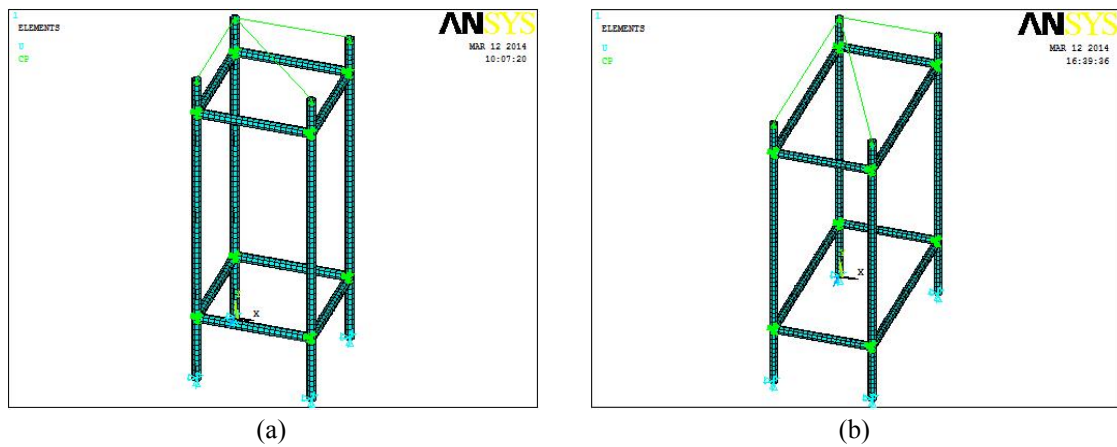


Fig. 11 The semi-rigid finite element models of the unit frames

### 3.2 Numerical results

#### 3.2.1 Ultimate vertical bearing capacity

The British Standard 5975 defines 1% defect as the initial geometric imperfection in nonlinear buckling analysis, due to the defects and the irregular shape of specimen materials (The rods are standardized production, while their lengths are differential. Hence, the unit frame erected by the rods twists in the loading process). The nonlinear ultimate vertical bearing capacity of each specimen, and the contrast of the numerical to the experimental results are shown in Table 4 and Fig. 12.

Table 4 shows that the numerical results obtained by the two-linear reinforcement model are similar to the experimental results; the wedge head in specimen 4 slid out and could no longer bear loads during the experiment, while in numerical analysis its translational freedom of the nodes are coupled. Hence, the numerical result of specimen 4 is larger than the experimental one. The influence of node connection stiffness to the vertical bearing capacity had nothing to do with  $h_1$  in numerical analysis, while that influence depended on  $h_1$  in the experiment.

The numerical results of specimens 1-3 differ from the experimental results. Major causes were boundary conditions, experiment deviation, and incidental factors. In numerical analysis, the boundary conditions of the finite element models couldn't be completely consistent with those of the experiment, and the difference inevitably created different results. The test device, structural dimension, and loading were not 100% accurate, so the finite element models suggested more perfection than the test frames, although we defined a 1% defect as the initial geometric imperfection in the analysis. Additionally, in testing there existed some incidental factors and uncertainties.

Table 4 Ultimate vertical bearing capacity in nonlinear analysis

Ultimate vertical bearing capacity/kN	Unit frame number			
	1	2	3	4
Experimental	351	283	234	153
Numerical	344	303	255	227
Differential rate of numerical to experimental	-2%	7%	9%	49%

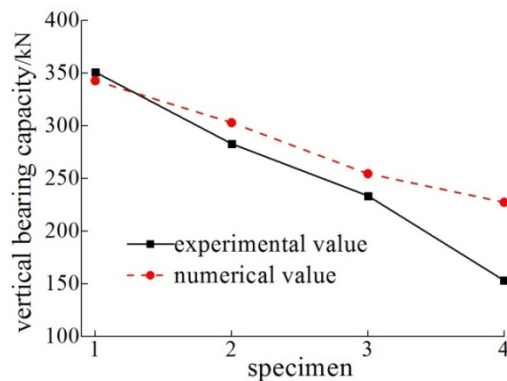


Fig. 12 Comparison of numerical analysis results to experimental ones

3.2.2 Load-deflection and buckling mode of the unit frames

Fig. 13 showed the load - deflection curves of the experimental results and the numerical results. In experimental results, the mechanical response before their ultimate bearing load of all

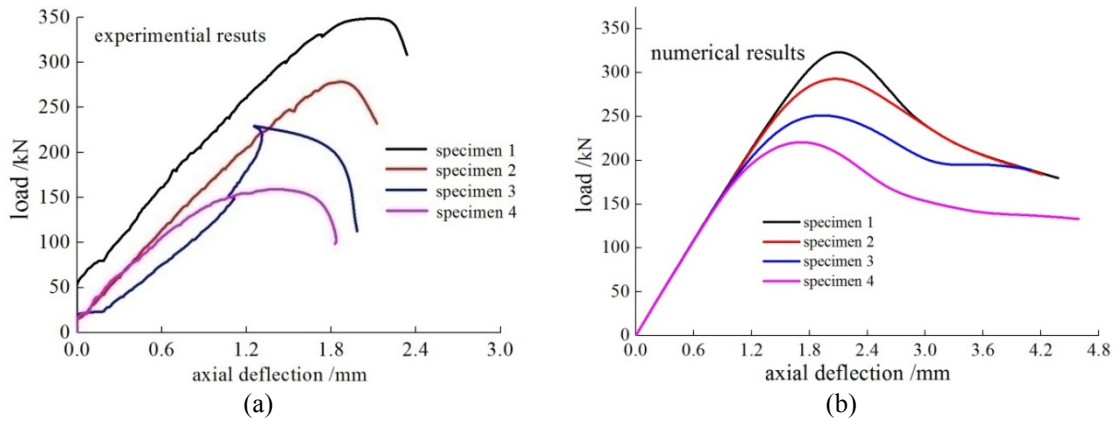


Fig. 13 Comparison of load-deflection

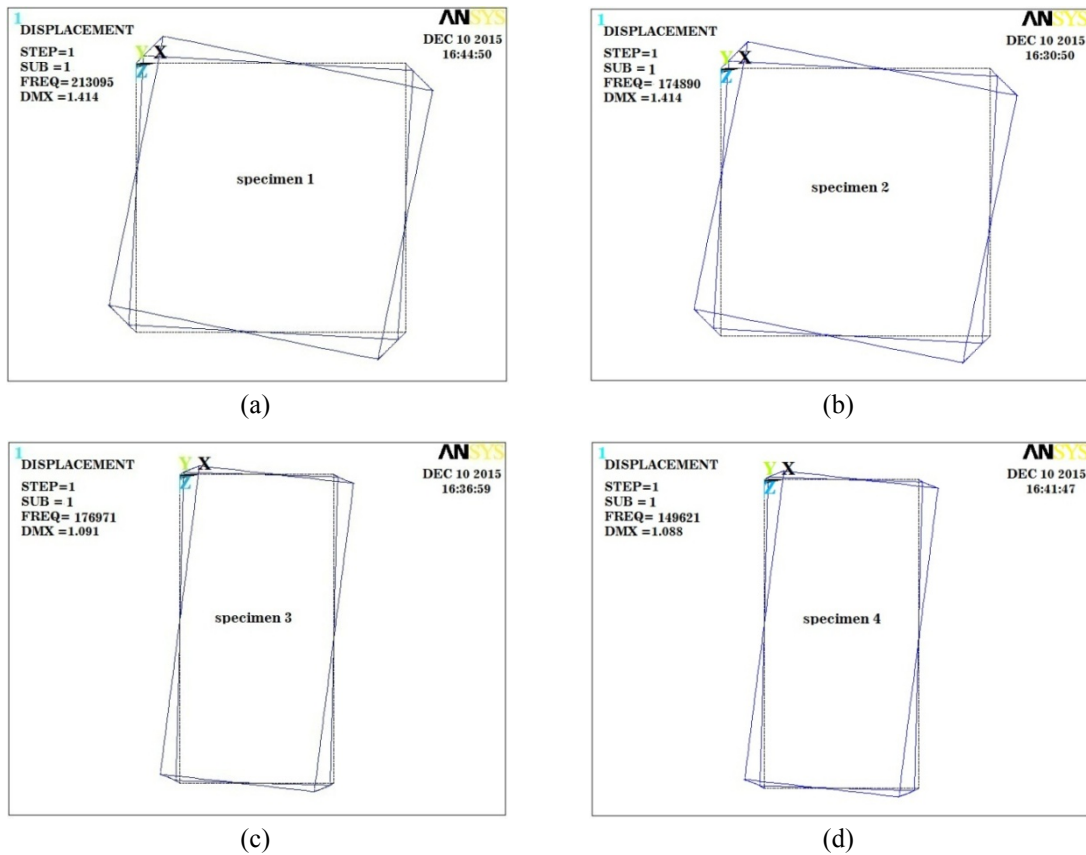


Fig. 14 The buckling mode of each unit frame in linear analysis (plan view)

the unit frames was similar to the maximum point instability, but after their ultimate bearing load, the unit frame failed rapidly and being instability. The numerical results of load - deflection curve was similar to the experimental one, unit frames still bearing load after the maximum point, and the stability state lasted longer than that in tests.

The curve in numerical analysis was integrated than the test as their perfect conformation, but the tendency of the curves was coincident, and they could simulate the tests under complicated conditions.

The failure mode of each unit frame was torsion in linear buckling analysis. As the same with experiment ones, different  $h_1$  and  $K$  values led to different deformation and torsional angles. The buckling modes in numerical analysis are shown in Fig. 14.

### 3.3 Numerical analysis of unit frames with other specifications

As the element size of the socket-type template supporting system was fixed, the numerical analysis of the vertical bearing capacity on four more unit frames was conducted with different specifications under normal and minimum wedge tightness. The specification of each unit frame is shown in Table 5. The height of the bottom horizontal tube, the length of the stud out, and the erection method are the same as those used in the experiment. 600 mm, 900 mm, and 1200 mm are the most commonly used lengths during the construction of concrete beams and slabs. Hence, the different combinations of the spacing of the upright tubes in the numerical analysis covered all the construction conditions.

The vertical bearing capacities of all the unit frames under nonlinear analysis are summarized in Table 6, put all the numerical results together can easier to comparison.

Based on the analysis, we drew the numerical vertical bearing capacity results of all the unit frames in Fig. 15 that were intuitive. From Fig. 15, we know that the ultimate bearing capacity reduces sharply if either  $h_1$  or  $h_2$  are greater than 900 mm. The ultimate bearing capacity is smaller when  $h_1$  is greater than  $h_2$ . For example, the bearing capacity of the unit frame with 900 mm × 1200 mm spacing is larger than that with 600 mm × 1200 mm.

Table 5 Specification of the unit frames in numerical analysis

No.	$h$ /mm	$h_2$ /mm	$h_1$ /mm	$K$
5	1200	600	900	Normal wedge tightness
6				Minimum wedge tightness
7		900	900	Normal wedge tightness
8				Minimum wedge tightness
9		900	1200	Normal wedge tightness
10				Minimum wedge tightness
11		1200	1200	Normal wedge tightness
12				Minimum wedge tightness

Table 6 Nonlinear bearing capacity of the unit frames

No.	1	2	3	4	5	6	7	8	9	10	11	12
Bearing capacity/kN	344	303	255	227	337	290	293	264	262	230	234	202

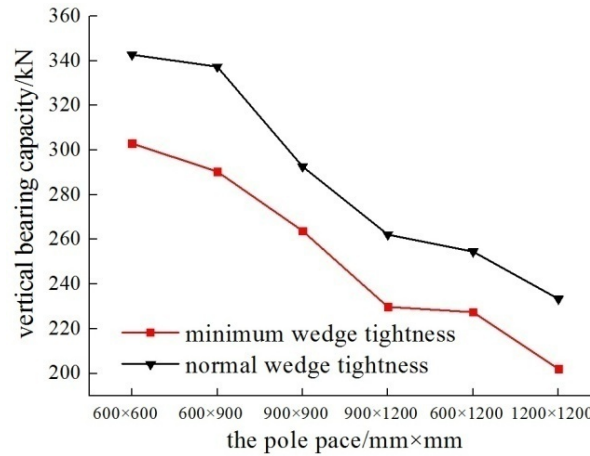


Fig. 15 The numerical vertical bearing capacity of the unit frames

### 3.4 Numerical analysis of the node domain

Analysis on the nodes of coupler tubular steel scaffold has been undertaken, (Chen *et al.* 2010). It shows that the junction cover plate, the base, the connection between the base and the cover plate, and the base plate are more stressed during the loading process. In this paper, we conducted nonlinear finite element analysis on the node of the socket-spigot template supporting system in order to discover the weaknesses of the node area under different stress states. The material parameters of node finite element model are shown in Table 3.

The socket-spigot template supporting system has kinds of usage in application, one is poles bearing load, the other is rod bearing load. We conducted nonlinear analysis of the model to obtain the primary stress area of the node under two conditions: a vertical load on the rod end with the two ends of the pole fixed, and a vertical load on the top of the pole with the pole bottom and the rod end fixed. In both conditions, the vertical load was defined as 1000 N, as shown in Fig. 16.

The displacement distribution and von Mises stress distribution under these two conditions are shown in Fig. 17, which shows that both sides around the plug hole are the primary bearing area when the load is transferred from the rod to the pole. The bearing area around the plug hole does

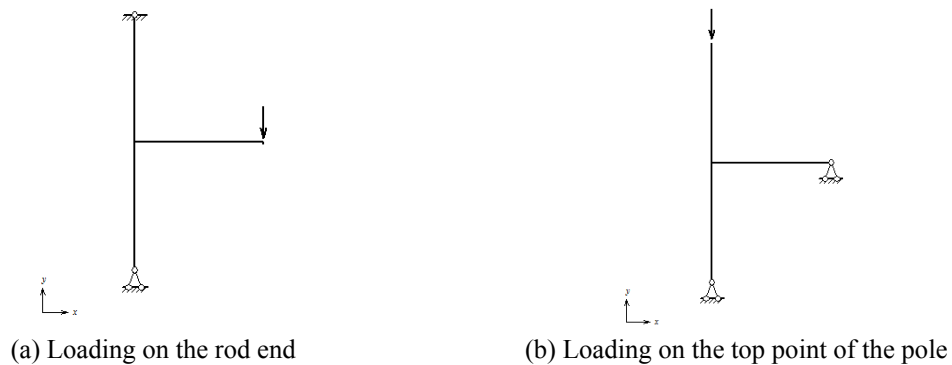
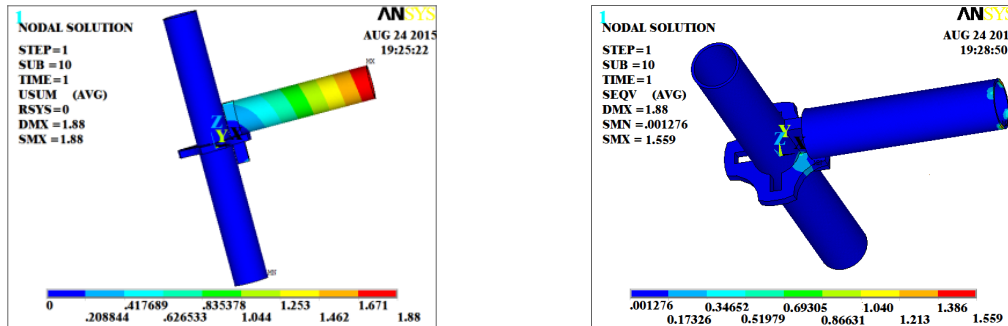
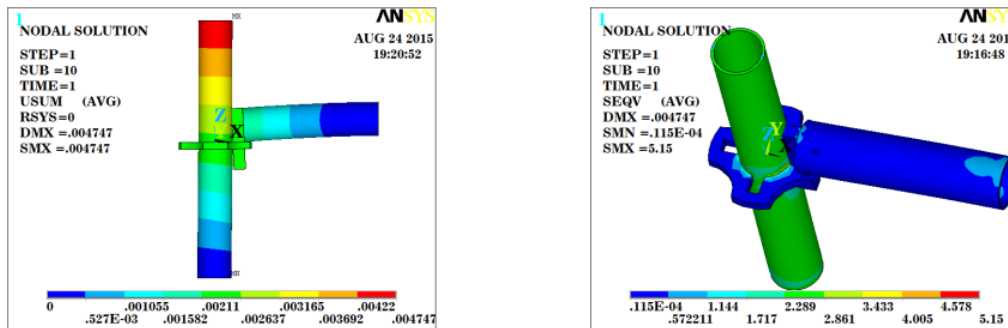


Fig. 16 Different ways of bearing load



(a) Stress with loading on the rod end



(b) Stress with loading on the top point of the pole

Fig. 17 The Von-Mises stress of the node

not transfer to the entire plate, and the connection region of the wedge head and the plate hole undergo the largest stresses. All the weld zones on the plate bear load when it is transferred from the pole to the rod. The wedge head bearing load is caused by extrusion, but it is transferred at a small scale; most of the vertical load is transferred along the pole. Therefore, the load transfer direction greatly affects the node bearing area, and we must determine the bearing scheme according to the specific conditions in each application.

#### 4. Application performance analysis

While the socket-spigot template supporting system is constructed efficiently and erected quickly, it does not meet the bearing demand under special situations with its fixed specification artifacts. Hence, we always mix the socket-spigot and fastener systems in scaffold applications.

##### 4.1 Test set-up

An on-site test was made of a mixed template supporting system under a long beam. The vestibular beam was 24 m in length, with an 1800 mm × 800 mm section, in a multi-function building. The slab alongside the beam was 120 mm in thickness. The supporting system under the beam was erected of socket-spigot and tubular scaffolds. Its  $h_1$  was 450 mm, and its  $h_2$  was 400 mm. The lift height was 1200 mm, and the total height was 9.2 m, as shown in Fig. 18. The socket

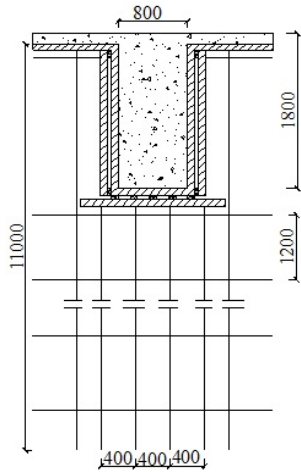


Fig. 18 Section of mixed scaffold under the beam

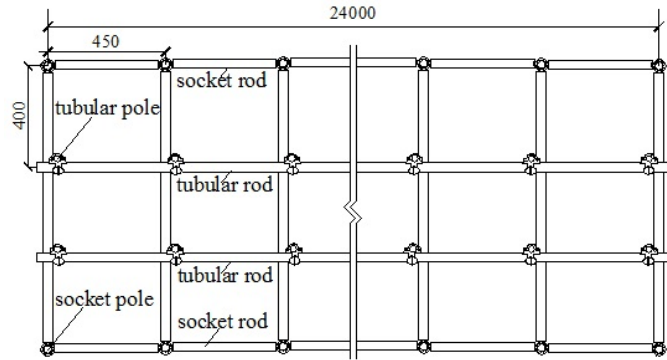
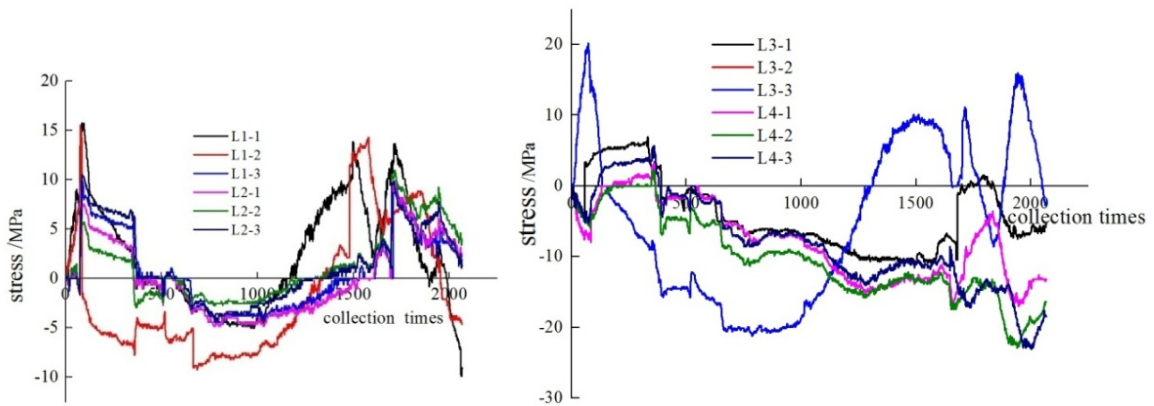
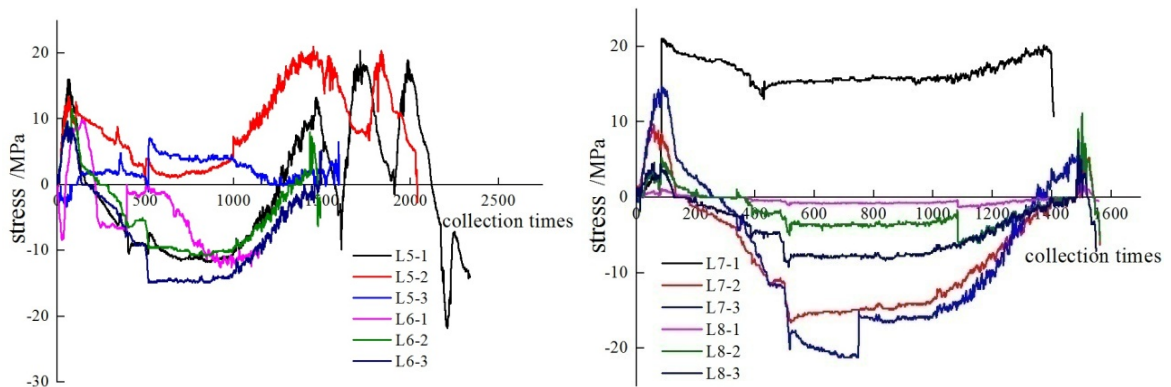


Fig. 19 Plan view of the supporting system



(a) Stress of pole measuring points in middle



(b) stress of pole measuring points in side

Fig. 20 Stress of pole measuring points

spigot scaffold was the main frame in the supporting system. Its  $h_2$  was 400 mm, and its longitudinal length was 450 mm. The tubular scaffold was the strength frame, as shown in Fig. 19.

The mixed supporting system was long and narrow. Hence, its horizontal bracing was connected to the inner supports to improve the overall stability. During the test, we measured the strain of the poles in the middle and on the sides, of the bottom rod, of the top rod, and of the bracing. In total, we monitored four socket poles, four tubular poles, one socket rod, one tubular rod, one horizontal bracing, and one vertical bracing. Each element had three measuring points.

#### 4.2 Analysis of test results

The stress of each measuring point during the concrete pouring was gathered, and is shown in Figs. 20-22.

In Fig. 20, L1, L4, L5, and L8 are socket poles, and L2, L3, L6, and L7 are tubular poles. During the concrete pouring, the poles directly under the pouring area were in compression, with the maximum compressed stress being approximately 20 MPa. The poles away from the pouring area bear load when the pouring begins. Some of the poles were in tension, with a maximum tensile stress of 20 MPa. The pole tensile stress was of short duration, and it mutated to compressive stress while concrete was being poured. The stress of the lower measuring point was generally smaller than that of the upper point in the same pole. The larger stress occurred at the point closer to the pouring surface, and the stress trends of different measuring points in one pole were the same. The stress of the socket pole was larger than that of the tubular pole in the same row, which shows that the socket pole plays a major role in the structure.

In Fig. 21, H1, H2, and H3 are the socket rods that were located in the longitudinal direction. H4, H5, and H6 are the tubular rods that were located in the horizontal direction. The rod stress was small before concrete pouring began, and it changed continuously during pouring. The socket rod was in compression during pouring, but in tension during maintenance. The tubular rod, on the contrary, was in tension all the time.

In Fig. 22, AJ1, AJ2, and AJ3 are the horizontal bracing points, while BJ1, BJ2, and BJ3 are the vertical ones. During construction, the stresses at the horizontal bracing measuring points were larger than those of the vertical ones, as the horizontal bracing was connected to the internal support. The maximum stress was about 20 MPa. The stresses of the vertical bracing measuring

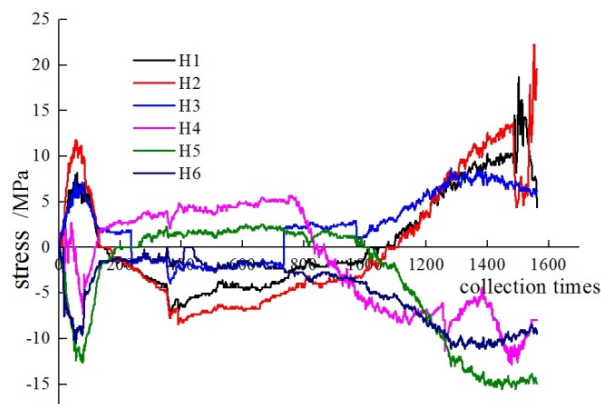


Fig. 21 Stress of rod measuring points

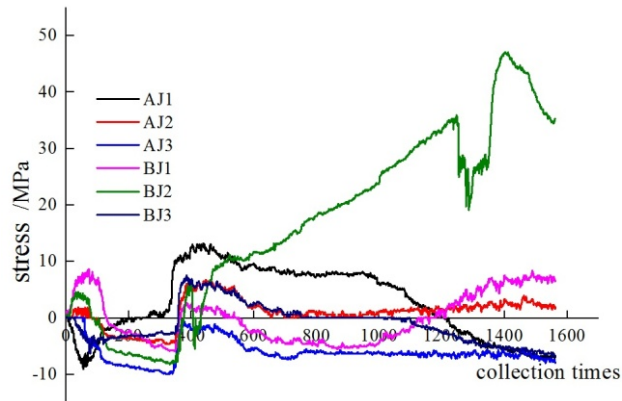


Fig. 22 Stress of bracing measuring points

points BJ1 and BJ3 were small, while the bracing reinforced the existing column at measuring point BJ2. Hence, its tensile stress was larger.

## 5. Conclusions

Based on the vertical bearing capacity experiment of the unit frames of a socket-spigot template supporting system, we investigated the influence of  $h_1$  and  $K$  on the ultimate vertical bearing capacity, obtaining the following conclusions by experiments and numerical analysis:

- $h_1$  and  $K$  influence the vertical bearing capacity in a socket-spigot template supporting system. The influence of  $K$  on the vertical bearing capacity depends on  $h_1$ . The larger  $h_1$  is, the more significant is the influence of  $K$ .
- The pole displacement increases instantly when it reaches the ultimate bearing capacity. The unit frame is damaged with clockwise torsion, and the degree of deformation of each pole is different. We should estimate the bearing capacity of supporting systems used in real-world applications to prevent their collapse.
- The load of the rod is transferred by the wedge head. Hence,  $K$  influences the rod displacement development and the node stiffness.
- The unit frame is destroyed through instability, rather than buckling, under vertical load without surrounding support. We should avoid overly large values of  $h_1$ , or the lateral stiffness will differ more in construction, causing instability. In addition, we should ensure the node connection quality when  $h_1$  is large.
- The longitudinal and transverse stiffness affects the bearing capacity of the supporting system. The larger the difference is between them, the smaller the bearing capacity will be. Thus, we should connect the weaker side to the existing structure during construction, when the supporting system is long and narrow.
- The load transfer direction influences the joint bearing plate area directly. Therefore, different template supporting schemes will produce different mechanical responses.
- We can analyze the bearing capacity of the socket-spigot template supporting system in advance, and determine the weak points of the template supporting system and enhance it, in order to ensure its safety in actual applications.

## Acknowledgments

The authors are grateful for the National Natural Science Foundation of China(Grant No. 50978219) and the Education Department of Shaanxi Provincial Government(Grant No. 12Jk0898). Thanks also go to Mike Brewes, retired instructor from Nipissing University, Canada for his assistance in proofreading this article.

## References

- Adam, J.M., Pallarés, F.J., Calderón, P.A. and Payá, I.J. (2007), “A study of the conditions of use of a new safety system for the building industry”, *Eng. Struct.*, **29**(8), 1690-1697.
- Beale, R.G. (2014), “Scaffold research — A review”, *J. Construct. Steel Res.*, **98**, 188-200.
- British Standard 5975 (1996), Code of practice for false work, London, UK.
- Chandrangsu, T. and Rasmussen, K.J.R. (2011a), “Investigation of geometric imperfections and joint stiffness of support scaffold systems”, *J. Construct. Steel Res.*, **67**(4), 576-584.
- Chandrangsu, T. and Rasmussen, K.J.R. (2011b), “Structural modelling of support scaffold systems”, *J. Construct. Steel Res.*, **67**(5), 866-875.
- Chen, Z.H., Lu, Z.R. and Wang, X.D. (2010), “Numerical analysis and experimental study of the stiffness of right angle couplers in tubular steel scaffolds”, *China Civil Eng. J.*, **104**(9), 100-108.
- Peng, J.L., Chan, S.L. and Wu, C.L. (2007), “Effects of geometrical shape and incremental loads on scaffold systems”, *J. Construct. Steel Res.*, **63**(4), 448-459.
- Peng, J.L., Wu, C.W. and Chan, S.L. (2013), “Experimental and numerical studies of practical system scaffolds”, *J. Construct. Steel Res.*, **91**, 64-75.
- Weesner, L.B. and Jones, H.L. (2001), “Experimental and analytical capacity of frame scaffolding”, *Eng. Struct.*, **23**, 592-599.
- Yu, Z.M. (2001), *Configuration Theory and Safe Application of New Type Scaffolds*, China Railway Press, Beijing, China.
- Zhang, H., Rasmussen, K.J.R. and Ellingwood, B.R. (2012), “Reliability assessment of steel scaffold shoring structures for concrete formwork”, *Eng. Struct.*, **36**, 81-89.
- Zhang, H. and Rasmussen, K.J.R. (2013), “System-based design for steel scaffold structures using advanced analysis”, *J. Construct. Steel Res.*, **89**, 1-8.